Identifying Coherence Across End-of-Century Montane Snow Projections in the Western United States

Justin M. Pflug[1,2], Sujay V. Kumar[1], Ben Livneh[3], Ethan D. Gutmann[4], Sudershan Gangrade[5,6], Shih-Chieh Kao[5,6]

[1]Hydrological Sciences Laboratory, NASA Goddard Space Flight Center, Greenbelt, Maryland
[2]Earth System Sciences Interdisciplinary Center, University of Maryland, College Park, College Park, Maryland
[3]Cooperative Institute for Research in Environmental Sciences, University of Colorado, Boulder, Boulder, Colorado
[4]National Center for Atmospheric Research, Boulder, Colorado
[5]Environmental Sciences Division, Oak Ridge National Laboratory, Oak Ridge, Tennessee
[6]Climate Change Science Institute, Oak Ridge National Laboratory, Oak Ridge, Tennessee

Corresponding author: Justin M. Pflug (jpflug@umd.edu)

Key points:

- The relationship between snow projections had similar patterns with increases in elevation in five montane domains
- Projection magnitude and spread were used to benchmark when and where end-of-century changes to SWE were larger than model disparity
- Model coherence can be used to identify the locations of greatest projection confidence, and where improvements would be most beneficial

Abstract:

Montane snowpack is a vital source of water supply in the Western United States. However, the future of snow in these regions in a changing climate is uncertain. Here, we use a large-ensemble approach to evaluate the consistency across 124 statistically downscaled snow water equivilent (SWE) projections between end-of-century (2076 – 2095) and early 21st century (2106 – 2035) periods. Comparisons were performed on dates corresponding with the end of winter (15 April) and spring snowmelt (15 May) in five western US montane domains. By benchmarking SWE climate change signals using the disparity between snow projections, we identified relationships between SWE projections that were repeatable across each domain, but shifted in elevation. In low to mid-elevations, 15 April average projected decreases to SWE of 48% or larger were greater than the disparity between models. Despite this, a significant portion of 15 April SWE volume (39 – 93%) existed in higher elevation regions where the disparities between snow projections exceeded the projected changes to SWE. Results also found that 15 April and 15 May projections were strongly correlated ($r \geq 0.82$), suggesting that improvements to the spread and certainty of 15 April SWE projections would translate to improvements in later dates. The results of this study show that large-ensemble approaches can be used to measure coherence between snow projections and identify both 1) the highest-confidence changes to future snow water resources, and 2) the locations and periods where and when improvements to snow projections would most benefit future snow projections.

Plain Language Summary:

A significant portion of the Western United State's water originates from mountain snowpack.This study combines a large set of snow projections generated using different modeling approaches to determine 1) where snow projections agree, and 2) the proportion of snow that falls within regions where end-of-century projections of snow disagree. Results show that while a majority of the area in the interior Rocky Mountains and Washington Cascade mountain range have snow projections that agree, most of the annual snow water supply exists in the highest elevations where estimates of end-of-winter snowpack diverge. This study highlights the similar patterns of snow projection disparities, and the locations where further research may most improve our confidence in future snow water supplies.

1. Introduction:

Seasonal snow in mountainous terrain is a crucial source of water storage, providing runoff throughout the spring and summer snowmelt periods for agriculture, human consumption, industry, energy production, and ecosystems. In the Western United States, a majority of annual runoff is sourced from snowmelt (Li et al., 2017), but the volume and timing of snowmelt will change with projected changes to climate (e.g., Alder and Hostetler, 2019; Barsugli et al., 2020; Fyfe et al., 2017; Gergel et al., 2017; Ghan and Shippert, 2006; Ikeda et al., 2021; Leung et al., 2004; Li et al., 2017; López-Moreno et al., 2017; McCrary and Mearns, 2019; Qian et al., 2010; Rasmussen et al., 2014; Rhoades et al., 2018b, 2018a; Ullrich et al., 2018). Siirila-Woodburn et al. (2021) estimated that 78 – 94% of Western US regions in the second half of the century (2050 – 2099) will have 70% or larger declines to peak snow water equivalent (SWE), and annually-persistent low snow conditions emerging within the next 35 – 60 years. Historical snow observations in the Western U.S. have also confirmed climate change's impact on the volume of annual SWE accumulation, the frequency of snowfall and rainfall, and the timing of spring snowmelt onset (Hamlet et al., 2007; Harpold et al., 2012; Kapnick and Hall, 2012; Mote et al., 2018; Musselman et al., 2021).

Changes to the volume and timing of montane snowpack threaten local ecosystems and alter how water is partitioned between the land surface, evapotranspiration, and streamflow (Barnett et al., 2005; Hale et al., 2022; Harpold and Brooks, 2018; Musselman et al., 2017), making this information crucial for operational and policy decisions. Despite this, projections of future snow water resources are uncertain in montane regions. One of the greatest drivers of this uncertainty is the mismatch in spatial scales between the spatial heterogeneity of snowpack and the scale of climate projections. For instance, global climate models (GCMs) discretize the land surface at spatial scales much coarser (e.g., 50 – 200 km) than the variability of the topography in mountain terrain. These models commonly misrepresent the snow evolution that occurs in higher-elevation and snow dominated terrain, which may account for a small areal fraction of a GCM grid cell, but a large portion of that grid cell's snow volume. Misrepresentations of the spatial heterogeneity of snow and topography in the GCMs can also have key feedback on montane climate through processes like snow albedo feedbacks (Walton et al., 2017), and meteorological processes like mountain-pass air mixing, orographic gradients, rain shadows, and barrier jets (e.g., Guan et al., 2016; Hughes et al., 2009; Lundquist et al., 2010).

Snow evolution is also sensitive to processes like air temperature gradients and terrain shading, both of which occur at length-scales much smaller than the spatial resolution of GCMs (Clark et al., 2011). To represent these processes, it is common practice to downscale climate projections. To date, dynamic and statistical downscaling are the two most common downscaling approaches. Dynamic downscaling leverages the use of weather prediction models to more directly simulate the interactions between the coarser-scale climate projections and the underlying terrain. This approach resolves local weather patterns in a way that is not strictly correlated with local terrain features, but instead attempts to resolve the meteorological impacts that could occur from the interconnectedness of the land-atmosphere system (Gutmann et al., 2012; Minder et al., 2016; Walton et al., 2017). However, dynamic downscaling approaches are computationally expensive, and often still misrepresent the land surface conditions, interactions between the land surface and atmosphere, and the resulting local meteorological conditions in mountainous terrain (e.g., Aas et al., 2017; Le Roux et al., 2018; Xue et al., 2014). In this study, we focus on statistically downscaled snow projections which are less computationally expensive and more common in practice. Statistical downscaling derives finer resolution meteorology using the relationship between GCMs and reference meteorological datasets in historical periods (e.g., Abatzoglou and Brown, 2012; Hidalgo et al., 2008; Orlowsky et al., 2010; Pierce et al., 2014; Wood et al., 2004). However, this approach assumes that the reference datasets are accurate when in reality, there are often biases in these datasets, particularly in remote and high-elevation montane regions (e.g., Currier et al., 2017; Lundquist et al., 2015; Wayand et al., 2013). Statistical downscaling also assumes a static relationship between the GCM output and finer-scale reference dataset, when this relationship could change in time with a changing climate.

Even if credible meteorological forcings are available, modeling decisions have impacts on estimates of snow evolution in complex terrain (Chegwidden et al., 2019; Srikrishnan et al., 2022). Most snow projections simulate snow using spatiotemporally continuous climate projections. However, other approaches have used the delta-method (e.g, Barsugli et al., 2020; Sofaer et al., 2017), where monthly or more-frequent perturbations are made to a historical record of climate (e.g., 20 – 30 years) based on average projected changes to meteorological variables (e.g., temperature, precipitation, etc.). This approach prescribes future simulations with the interannual variability from the historical climate record, but more-explicitly relates the difference in modeled state variables to average changes in meteorological conditions. Different land surface and snow models are also subject to different parameterizations and modeling decisions, such as rain and snow thresholding, canopy interception, wind-redistribution, and liquid water percolation. These parameterizations cause snow simulations across different models to diverge from each other (Essery et al., 2013; Jennings et al., 2018; Lumbrazo et al., 2022; Pflug et al., 2019; Reynolds et al., 2021). In fact, some studies have documented that the differences between snow models cause snow simulations to differ by greater amounts than different meteorological forcing datasets (Kim et al., 2021; Mudryk et al., 2015).

Different combinations of GCMs, downscaling approaches, and modeling decisions can have interconnected and cascading impacts on model estimates of snow evolution. This makes the sensitivities and sources of disparities between projections using different modeling approaches difficult to attribute. Studies that analyze sensitivities to different model decisions often use a central model setup with limited and user-defined changes to modeling decisions like downscaling techniques, process parameterizations, or spatial resolutions (Abatzoglou and Brown, 2012; Alder and Hostetler, 2019; Barsugli et al., 2020; Gutmann et al., 2014; Hughes et al., 2017). However, this could underestimate snow projection sensitivity by neglecting the compounding or compensating impacts that different sets of modeling decisions have (Essery et al., 2013; Raleigh et al., 2015). For example, a downscaling method that produces air temperatures closer to 0°C for a longer winter period may exhibit different sensitivities to a set of rain and snow partitioning functions than colder downscaled estimates of air temperature. Unfortunately, investigating the full interaction between multiple sets of modeling decisions often requires large numbers of simulations, which are computationally expensive for snow simulations over long-term future periods and mountain-range spatial extents.

Rather than diagnosing the sources of disparities discussed above, this study focuses on identifying the coherence, or the logical and consistent relationships between projected changes to snow across six snow projection ensembles with disparate modeling approaches and decisions.

This approach is motivated by model intercomparison studies like the Earth System Model Snow Model Intercomparison Project (ESM-SnowMIP; Krinner et al., 2018), which synthesizes information from a wide set of data sources to draw conclusions about the similarity of modeled hydrological states. Here, we focus on projected changes to end-of-century snow water resources in five Western U.S. montane domains spanning a variety of snow climates (Section 2). By benchmarking projected changes to SWE versus the disparities in SWE projections across different modeling approaches, we ask: **1) where and when do projected changes to montane snow water resources from different snow projections show consensus?, and 2) what proportion of snow water resources exist in the regions with snow projection disparities?** In doing so, we identify 1) the climate change signals of greatest confidence, and 2) the regions where future improvements in model coherence would most improve future projections of snow water resources.

2. Domains and data

2.1. Model domains and historical snow reanalyses

This project focused on five montane domains spanning a variety of snow climates and latitudes in the Western United States (Figure 1). These regions were chosen to focus on high-elevation domains with seasonal snowpack, with a special focus on the headwaters of snow reservoirs for the Colorado River and Columbia River basins. These domains also overlapped with known and proposed reintroduction habitat for snow-adapted species like the Canada lynx (*Lynx canadensis*) and North American wolverine (*Gulo gulo luscus*). Snow projections in this project were subset into five domains (Figure 1), labeled here as the Colorado (CO) Rockies (~118,000 km^2), Wyoming (WY) Rockies (~104,000 km^2), Montana (MT) Rockies (~80,000 km^2), Idaho (ID) Rockies (~31,000 km^2), and Washington (WA) Cascades (~31,000 km^2).

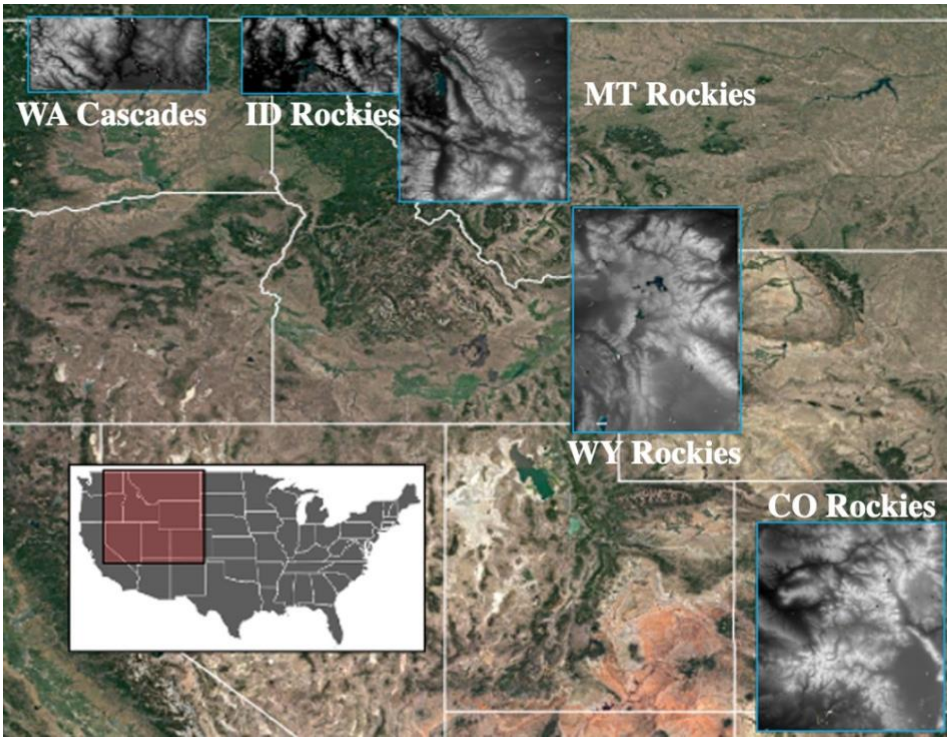

Figure 1. Western US montane study domains. Each domain is outlined in blue and is superimposed with a 0.01° grayscale elevation map.

Historical (1991 – 2021) SWE was defined from the Western United States UCLA Snow Reanalysis (Fang et al., 2022). This product generates SWE at daily timesteps and 16 arc-second (~500m) spatial resolution using an ensemble of snow simulations weighted towards annual observations of snow cover depletion from Landsat using a Bayesian smoother. This product is among the highest-accuracy estimates of SWE volume and distribution, demonstrating the capability to match in situ and airborne snow observations (Fang et al., 2020; Pflug et al., 2022). This data was used to provide an estimation of average historical snow distribution in each domain, that was independent from the snow projections compared here (Sections 2.2 and 2.3), as a basis for highlighting the proportion of each domain's snow water resources that exist in regions with various levels of agreements and disparities across the snow projections.

2.2. Novel montane snow projections

Two snow projections were created for this study. A detailed description of these projections can be found in Text S1. These projections were performed using a two-step modeling approach which 1) developed a baseline simulation representative of snow evolution in a historical period between 1995 and 2016 using forcing downscaled from MERRA2 (Gelaro et al., 2017) with additional precipitation calibration, and 2) perturbed the MERRA2 baseline simulation with future climate-change signals. While straightforward, this change-factor approach (also termed the *delta method*) is a reliable approach for determining hydrological and ecological climate sensitivities (Barsugli et al., 2020; Sofaer et al., 2017). In this study, future climate change signals were derived from NASA Earth Exchange Global Daily Downscaled Projections (NEX-GDD-CMIP6; Thrasher et al., 2022), which downscaled climate projections from the Coupled Model Intercomparison Project phase 6 (CMIP6; Eyring et al., 2016) using the popular bias correction spatial disaggregation (BCSD) approach (Wood et al., 2004) and reference historical meteorological data from the Global Meteorological Forcing Dataset (GMFD; Sheffield et al., 2006). Readers are referred to Thrasher et al. (2022) and Wood et al. (2004) for more information on NEX-GDDP-CMIP6 and BCSD, respectively.

Using variogram analysis, we determined that the interannual variability in domain-mean winter air temperature and precipitation for both the historical snow simulation and NEX-GDDP-CMIP6 data plateaued for 14 – 18 year periods (e.g., Subyani, 2019) (Text S1). Beyond 18 years, the change to domain mean temperature and precipitation were more driven by climate trends. To be conservative, we partitioned the historical and future climate records into 20-year windows. Since the CMIP6 “historic” data record runs from January 1950 to December 2014, the 20-year historical period for this study spanned from October 1994 to September 2014 (water years 1995 to 2014). We then partitioned 20-year increments forward in time from the historic record. Here, we focus on 20-year data records from an early 21st century period (2016 – 2035) and end-of-century period (2076 to 2095). Monthly maps of change-signals in air temperature, specific humidity, shortwave radiation, longwave radiation, wind speed, surface pressure, and precipitation were then calculated for both the early 21st century and end-of-century periods from the NEX-GDDP-CMIP6 data in those periods, relative to the historical period.

Finally, SWE projections were performed using two different approaches. First, model forcing from the 20-year historical simulations between 1995 and 2014 was perturbed with average monthly 0.01° climate change signals aggregated from the NEX-GDDP-CMIP6 data in the early 21st century and end-of-century periods. This simulation is referenced in this manuscript by NEX6-C ("C" indicating that climate perturbations were performed in the 20-year *continuous* simulation). The second simulation used the median forcing aggregated at daily timesteps for each grid cell over the 20-year historical period. This simulation was then perturbed using the same monthly climate change signals from NEX-GDDP-CMIP6. This simulation is referenced by NEX6-M ("M" indicating that simulations were performed using 20-year *median* forcing).

The difference between the NEX6-C and NEX6-M simulations, which were perturbed using the same climate change signals, were indicative of uneven climate change impacts on subsets of years. For example, grid cells where NEX6-C projections that had end-of-century projected SWE decreases that were larger than NEX6-M projections indicated that climate impacts on SWE in these grid cells were disproportionately large in low snow years, as compared to years with average snow conditions. This is discussed more in the study Results (Section 4) and Discussion (Section 5). More information on the NEX6-M and NEX6-C snow projections can be found in Text S1.

2.3. Similarities and differences across novel and existing snow projections

The snow projections discussed in Section 2.2 were compared with four additional statistically-downscaled snow projections from the literature (Abatzoglou et al., 2014; Brekke et al., 2013; Kao et al., 2022a; Vano et al., 2020). Information on each of these snow projections, and the citations discussing each can be found in Table 1. Each snow projection dataset was labeled using an acronym representative of the combination of the statistical downscaling and the CMIP phase (Table 1). However, the commonalities and differences in modeling decisions among the snow projection datasets go beyond the differences in CMIP phases and downscaling approaches. For example, although three projection datasets use CMIP6 projections and three use CMIP5 projections, identical sets of GCMs are only used by 1) NEX6-M and NEX6-C, and 2) LOCA5 and BCSD5. More information on the GCMs used by each projection dataset can be found in Text S2. Half of the datasets use the BCSD downscaling (NEX6-M, NEX6-C, and BCSD5). However, four unique reference datasets are used to downscale these climate projections compared here, all of which are at different spatial resolutions. Although snow projections are generated using only two different land surface models, different model parameterizations and calibrations were used. Here, the cascading differences in the projections, GCMs, and downscaling decisions in Table 1 alter the model forcing applied for each model ensemble member.

As discussed in Section 1, differences in modeling methods make the differences across projection datasets difficult to attribute, and often even more difficult to determine what approaches are better and worse than others. For example, assuming that the differences in the snow projections compared here can be attributed to only the GCMs used by the snow projections (Text S2), and the degrees of freedom in modeling decisions listed in Table 1 (four statistical downscaling approaches, four reference datasets, two time discretizations, and two land surface models), a full sensitivity analysis covering all possible combinations of GCMs and modeling decisions would result in 3,520 separate projections. Given this, we hypothesize that the snow and climate research communities may benefit most from studies that evaluate where and when disparate modeling decisions approach common results, and the consequences of uncertainties in locations where models disagree the most. This study focuses on six snow projection methodologies outputting 124 different snow projections. Our approach for comparing these projections is covered in Section 3 below.

Table 1. Selection of the differences between the snow projection datasets compared in this study. More information on these projections, and how the NEX6-M and NEX6-C projections were generated can be found in Text S1 and Text S2.

Dataset	Climate forcing	Downscaling: Statistical approach	Downscaling: Reference dataset	Downscaling: Resolution	Climate perturbation	Land surface model
NEX6-M *(Section 2.2)*	CMIP6; *Climate Model Intercomparison Project, phase 6*	BCSD; *Bias Correction and Spatial Disaggregation (Wood et al., 2004)*	GMFD; *Global Meteorological Forcing Dataset (Sheffield et al., 2006)*	1/100°	Delta method *(Sofaer et al., 2017)*	Noah-MP *(Niu et al., 2011)*
NEX6-C *(Section 2.2)*	CMIP6	BCSD	GMFD	1/100°	Delta method	Noah-MP
DBCCA6 *(Kao et al., 2022)*	CMIP6	DBCCA; *Double Bias Corrected Constructed Analogues (Werner and Cannon, 2016)*	Daymet (Thornton et al., 2021)	1/24°	Continuous	VIC; *Variable Infiltration Capacity model (Liang et al., 1994)*
BCSD5 *(Brekke et al., 2013)*	CMIP5; *Climate Model Intercomparison Project, phase 5*	BCSD	Maurer et al. (2002)	1/8°	Continuous	VIC
LOCA5 *(Vano et al., 2020)*	CMIP5	LOCA; *Localized Constructed Analogues (Pierce et al., 2014)*	Livneh et al. (2015)	1/16°	Continuous	VIC
MACA5 *(Abatzoglou et al., 2014)*	CMIP5	MACA; *Multivariate Adaptive Constructed Analogs (Abatzoglou and Brown, 2012)*	Livneh et al. (2015)	1/16°	Continuous	VIC

3. Methods

This study was designed to investigate 1) the shift in end-of-century projected SWE within each snow projection dataset, and 2) the disparity in projected changes to SWE between the projection datasets. Our comparisons were limited to the RCP 4.5 (CMIP5) and SSP2-4.5 (CMIP6) emission scenarios, which represent moderate, "middle-of-the-road" estimates of future emissions, global populations, and climate adaptation inequities (IPCC, 2021). To compare continuous snow projections more fairly versus the 20-year median simulations from NEX6-M (Section 2.2), median SWE was calculated at the grid cell-level for each projection dataset across early 21st century (2016 – 2035) and end-of-century (2076 – 2095) periods. Here, we focused on the projected change to SWE on 15 April and 15 May. The 15 April date was chosen to correspond with a period that was near the conclusion of the early 21st century winter snow accumulation season, but late enough to ensure that the date of domain maximum SWE volume occurred prior to that date. The 15 May date was selected to correspond with the period approximately midway through the melt season based on the snow reanalysis dataset (Section 2.1). In the Western U.S., these dates (15 April and 15 May) correspond with reference dates used for assessing streamflow, water infrastructure management decisions, and snow refugia (e.g., Barsugli et al., 2020; Koster et al., 2010; Ray et al., 2020).

SWE projections for each period (2016 – 2035 and 2076 – 2095, 15 April and 15 May) were discretized in space using the native spatial resolution for each dataset (Table 1). Each projection dataset was also disaggregated to a 0.01° grid using nearest-neighbor downscaling. Comparisons between these two spatial discretizations allowed comparisons between the snow projection datasets on a common grid, and highlighted how different representations of the land surface terrain and vegetation impacted the physical processes that influenced snow evolution. For example, snow projections at coarser resolutions can smooth features like mountain peaks, which although small in areal extent, are colder than their surroundings and may therefore be less sensitive to projected increases in future temperatures.

The spread of SWE projections for each dataset (Table 1), 20-year period (early 21st century and end-of-century), and date (15 April and 15 May) was prescribed by the spread of GCMs (Figure 2). Provided the length of time between the early 21st century and end-of-century periods, we expect the differences in the GCM ensemble spread between the two periods to be driven more by differences in GCM physics than internal variability (Hawkins and Sutton, 2009; Lehner et al., 2020). We started by comparing the difference in the distributions of SWE between the two 20-year periods at each 0.01° disaggregated grid cell (Figure 2a). We used a non-parametric approach, wherein distributions of SWE with no overlap indicated the largest signal of change, and distributions of SWE with high degrees of overlap indicated little-to-no change. This measure represented how large and certain SWE changes were over time provided the spread in SWE estimates from the GCMs in each period. The non-parametric approach we used was motivated by the Mann-Whitney U test,

$$U_1 = n_1 n_2 + \frac{n_{1(n_1+1)}}{2} - \sum R_1, \tag{1}$$

$$U_2 = n_1 n_2 + \frac{n_{2(n_2+1)}}{2} - \sum R_2, \tag{2}$$

where subscripts 1 and 2 indicate the early 21st century (2016 – 2035) and end-of-century (2076 – 2095) periods, n indicates the number of GCMs, and R indicates the rank of each GCM, ranked from lowest to highest values, including both 20-year periods (Figure 2a, numbering). The difference between U_1 and U_2 represents the degree of overlap in the SWE distributions between the two periods. For example, if projected changes to climate cause the end-of-century distribution of SWE to fall completely outside of the SWE distribution from the early 21st century, then the disparity between the U values would be large, as U_2 and U_1 use the lowest-possible and highest-possible sum of ranks, respectively ($\sum R_1 \gg \sum R_2$). Conversely, grid cells with little-to-no change in SWE would approach similar sums of ranks ($\sum R_1 \approx \sum R_2$), and similar U values.

A similar approach was used to evaluate the disparity between projected changes to SWE (Figure 2b). Specifically, for each 0.01° grid cell and snow projection dataset, the SWE percent-difference was calculated for each GCM between the early 21st century and end-of-century periods. To fairly compare snow projections with different numbers of GCMs (n), we calculated a Normalized Overlap Statistic (NOS)

$$NOS = \frac{\min[U_1, U_2]}{U_1 + U_2}, \qquad (3)$$

where NOS approaching 0.0 indicates a large difference in the distribution of SWE between the two periods, and NOS approaching 0.5 indicates little-to-no difference. The NOS statistic was calculated at each 0.01° grid cell for 1) each snow projection dataset using SWE between the early 21st century and end-of-century periods (e.g., Figure 2a), and 2) for all combinations of two snow projection datasets using the SWE percent-change between the early 21st century and end-of-century periods (e.g., Figure 2b). The NOS statistic is discussed more in Section 5.

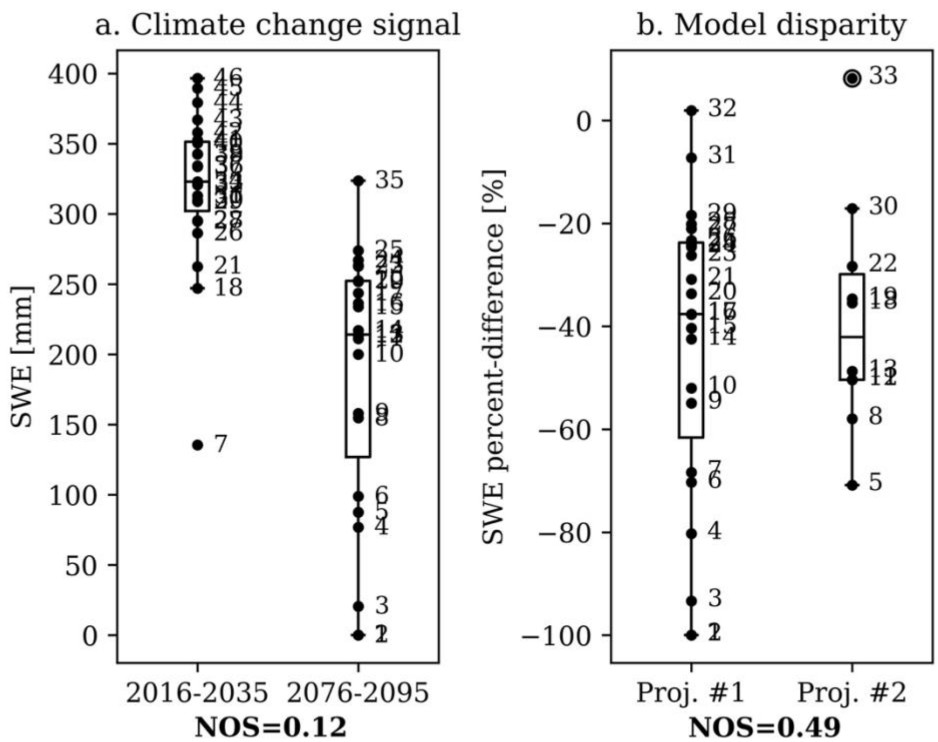

Figure 2. Conceptual demonstration of, a) the climate change signal on the SWE distribution over time for a single snow projection, and b) the difference in projected changes to SWE between two snow projections. Both subplots represent comparisons at a single 0.01° grid cell, with each scatter point representing a different GCM. Labels represent the ranks (*R* from Equations 1 and 2), and the NOS (Equation 3) for each comparison is labeled beneath the plot.

Finally, this study found that projected changes to SWE exhibited relationships with elevation in each domain. Therefore, statistics were aggregated over 100 m elevation bands. For each elevation band, we calculated the median and spread of 1) SWE percent-changes between the early 21st century and end-of-century periods, 2) NOS for changes to SWE in time for all projection datasets (termed *climate change signal*), 3) NOS for the differences to the projected changes to SWE between all combinations of two snow projections (termed *model disparity*), and 4) SWE from the Western US snow reanalysis (Section 2.1). We recognize that climate change signals (Figure 2a) and model disparities (Figure 2b) calculated using the NOS statistic are not independent of each other. Instead, these statistics were used together to benchmark the behavior of snow projections in time, relative to the disparities across the full set of snow projections. For example, elevations with model disparities (Figure 2b) that approached large NOS values represented SWE percent-changes that could not be easily differentiated between the different snow projections. If those same elevations also had climate change signals with low NOS values (e.g., Figure 2a), then the degree of change to SWE over time was large but in agreement across the different snow projection datasets. Here, by comparing these four data sources at each elevation band, we determined the volume of snow losses projected by each snow projection dataset, the SWE climate change signal relative to the disparity across models, and the amount of snow that historically existed in each elevation band. Together, these metrics were used to determine where *coherence*, or logical and consistent relationships across snow projections using disparate modeling approaches, and the portion of each domain's snow that falls within regions where snow projections agree and disagree.

4. Results

4.1. SWE projection comparisons, and relationships with elevation

Median projected changes to end-of-century SWE are shown for each domain and projection dataset on 15 April and 15 May in Figure 3 and Figure S1, respectively. The most visible differences between the snow projections in each domain were 1) differences in 2016 – 2035 snow extents (Figure 3, grid cells showing any projected change), and 2) disparities in the sign (positive/negative) and magnitude of projected changes to snow at the highest elevations of each domain. The Normalized Overlap Statistic (NOS, Equation 3) was able to highlight the similarities and differences in SWE projections, both within a given snow projection dataset over time (e.g., Figure 2a), and across multiple snow projection datasets (e.g., Figure 2b). For example, Figure 4 displays the 15 April NOS calculated across all grid cells in the WA Cascades domain. Contours in Figure 4 show the NOS values relative to the change in ensemble mean

SWE and SWE standard deviation between the early 21st century and end-of-century periods for each projection. Relative to the NEX6-M, NEX6-C, and MACA5 projections which projected both decreases and increases to end-of-century mean SWE, the BCSD5 and DBCCA6 models were dominated by grid cells with decreases to mean SWE and increases to the standard deviation of SWE across the GCMs. Despite this, the NOS exhibited similar patterns with changes to the mean and spread of SWE for each of the snow projection datasets (Figure 4, all-model average), with the smallest degree of overlap between early 21st century and end-of-century SWE (smallest NOS) occurring for grid cells with mean SWE decreases of 50 mm or more, and changes to SWE standard deviation between -50 mm and +100 mm.

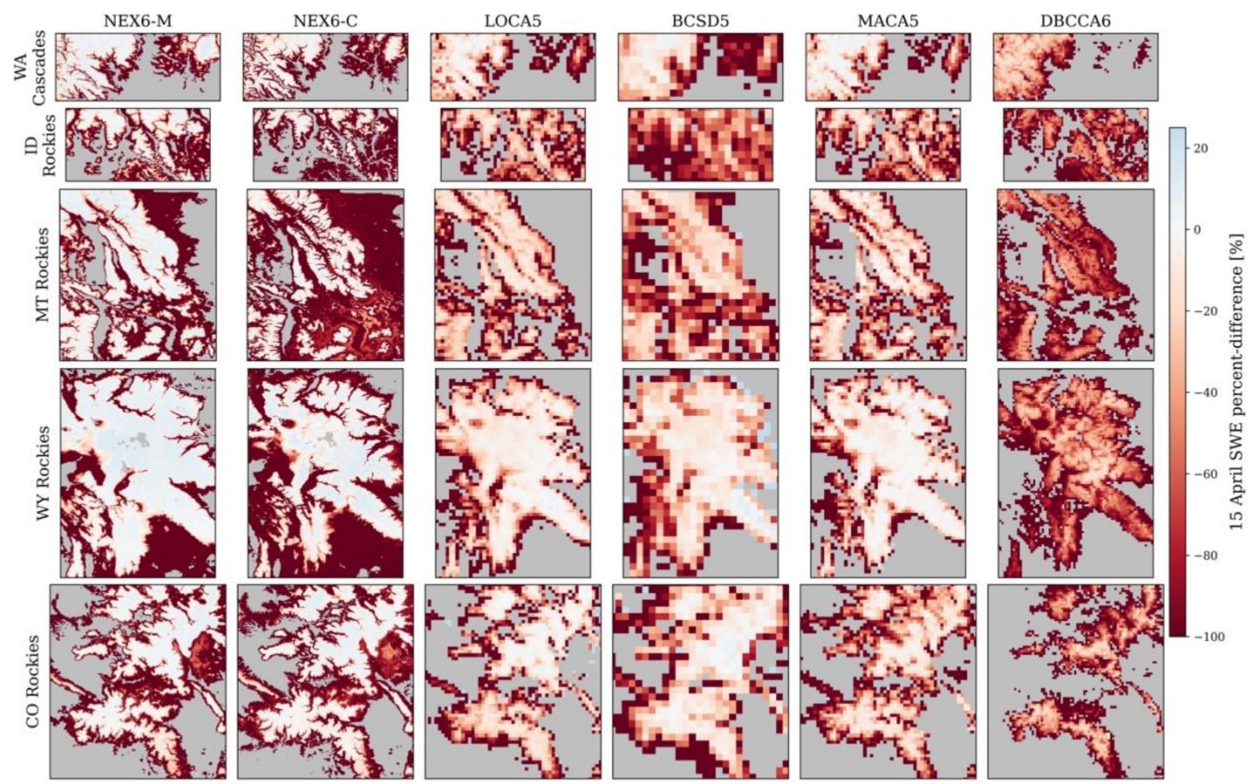

Figure 3. Spatial plots of median percent changes to 15 April SWE between an early 21st century (2016 – 2035) and end-of-century (2076 – 2095) period for five montane domains (rows) and six snow projection datasets (columns).

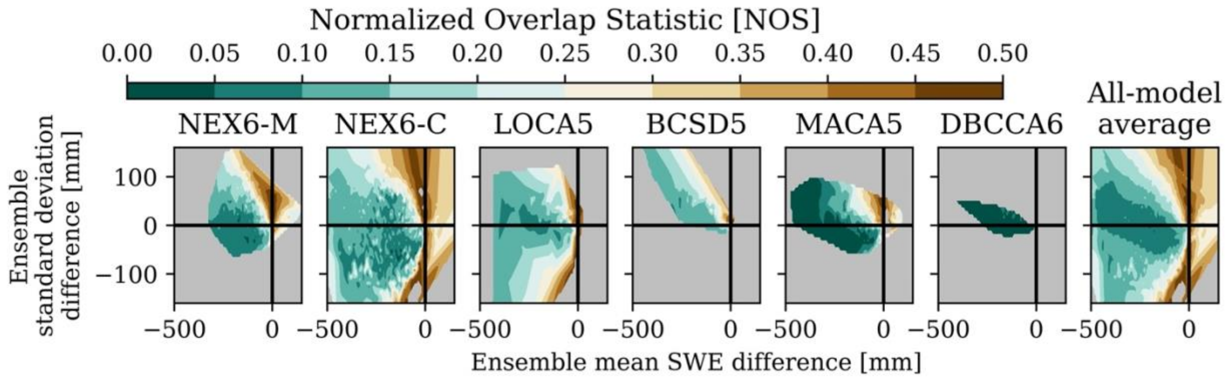

Figure 4. NOS (Equation 3) calculated between the early 21st century and end-of-century 15 April periods in the WA Cascades. Each subplot (projection dataset) is contoured based on the NOS values, ensemble mean SWE difference (x-axis), and ensemble SWE standard deviation difference (y-axis).

Projected percent-changes to 15 April SWE and the NOS statistic exhibited similar trajectories with increases in elevation in each domain (Figure 5, Figures S2 – S10). NEX6-C simulations commonly had the largest (in percent-difference) projected decreases to end-of-century snow at the lowest elevations of each domain, with median SWE changes between -87% and -100%, on average. Although the modeling approaches for the NEX6-M and NEX6-C projections were similar (Section 2.2), NEX6-M projected changes to SWE were among the most optimistic snow projections, with projected changes to SWE between -64% and -91% for the same low-elevation regions. At higher elevations, NEX6-M and NEX6-C simulations both exhibited steep gradients in SWE projections with changes in elevation. For example, in the WA Cascades domain, decreases to end-of-century SWE for both the NEX6-M and NEX6-C datasets decreased by approximately 12% for every 100 m increase in elevation between approximately 1350 and 1750m (Figure 5a). This gradient appeared in every domain for the NEX6-M and NEX6-C projections, varying in slope from approximately 8% (MT Rockies) to 17% (WY Rockies) per every 100 m in elevation. At elevations above these sharp gradients, NEX6-M and NEX6-C ensemble-medians projected either little-to-no change or increases to 15 April end-of-century SWE. Although the elevation at which median SWE first projected increases to 15 April SWE differed between the NEX6-M and NEX6-C projections, projected changes to SWE at the highest elevations of each domain typically agreed to within 5%.

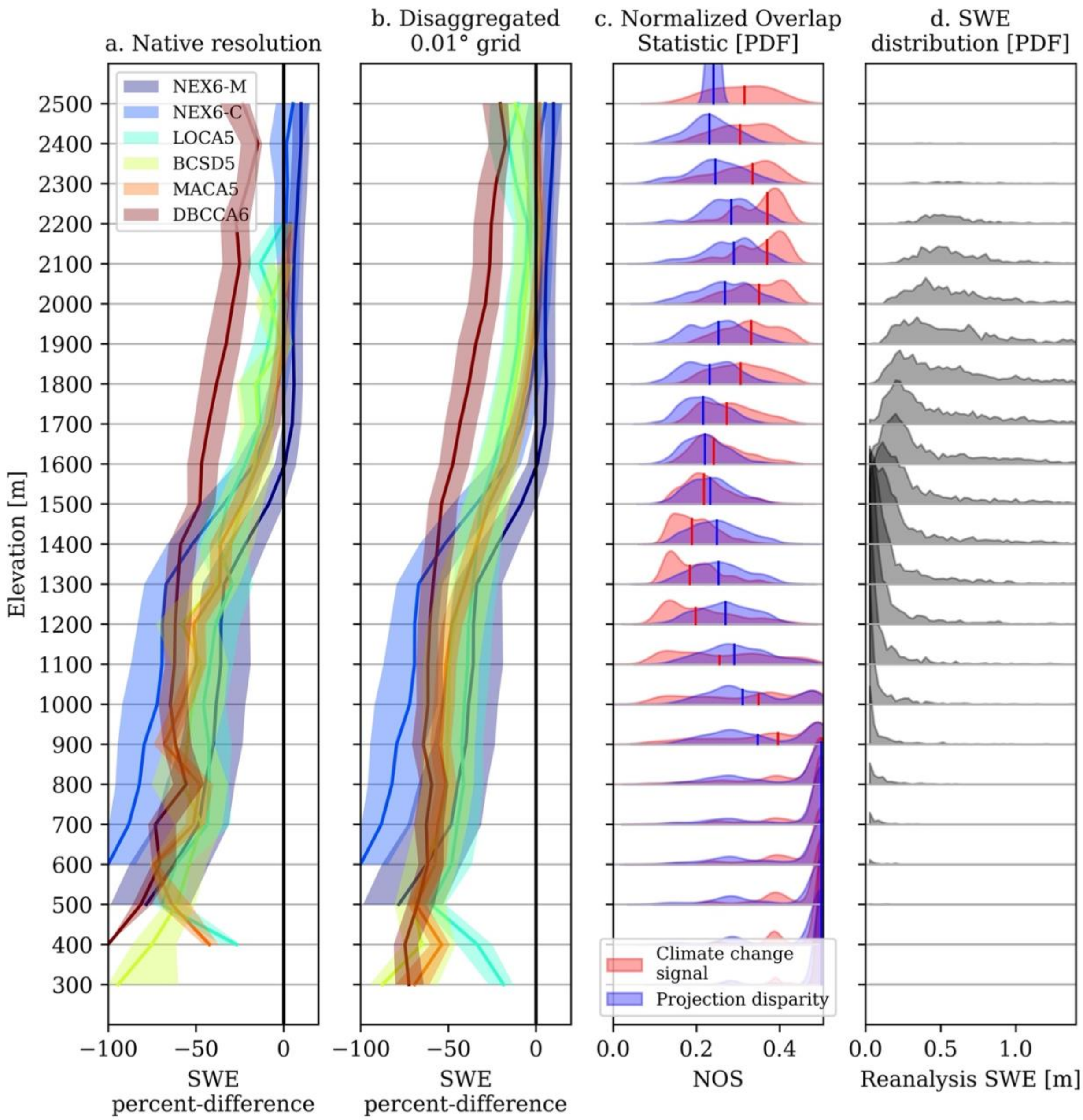

Figure 5. 15 April snow projections for the WA Cascades domain aggregated across 100 m elevation bands (y-axis). Subplots show the GCM median and interquartile spread of SWE percent-change from the native-resolution snow projection datasets (a), and the same statistics for the snow projection datasets disaggregated to 0.01° (b). The remaining subplots show the distribution and median of the NOS climate change and projection disparity signals (c), and the distribution of SWE from the snow reanalysis (d).

As opposed to the NEX6-M and NEX6-C projections, end-of-century 15 April SWE projections changed more gradually with increases in elevation for the LOCA5, BCSD5, MACA5, and DBCCA6 projections (Figure 5a, Figures S2 – S10, Table S1). At the lowest elevations of each domain, these projections typically estimated 15 April SWE decreases that fell near or within the bounds estimated from the NEX6-M and NEX6-C projections. Then, with every 100 m increase in elevation, 15 April SWE decreases changed between 2% and 4%, on average, for the LOCA5, BCSD5, and MACA5 projections. 15 April SWE for these datasets were either projected to decrease, or had smaller projected increases to SWE than the NEX6-M and NEX6-C projections at the higest elevations of each domain. Here, the DBCCA6 snow projections were consistently more pessimistic than the other projection datasets (Figure 5). In fact, in no domain did the DBCCA6 dataset project increases to 15 April SWE across any elevation band, and at the highest-elevations, DBCCA6 projected SWE losses ranging from -21% (CO Rockies) to -48% (WY Rockies).

As compared to the 15 April date, the SWE percent-difference on 15 May had larger projected decreases. This was expected since SWE projections on 15 May were influenced by both winter SWE change signals, like transitions from snowfall to rainfall and earlier snowmelt onset, in addition to increased rates of spring snowmelt driven by end-of-century increases in spring snowmelt energy and thinner snowpacks that melted more readily. The relationships between the SWE percent change and elevation discussed above exhibited similar patterns on both 15 April and 15 May. However, these patterns were shifted up in elevation with spring snowmelt. This caused nearly-linear relationships between the 15 April and 15 May SWE projections at common elevation bands (Figure 6), the slope of which was driven in large part by the 15 April SWE projections. For example, for the NEX6-M and NEX6-C projections, each domain exhibited decreases to end-of-century SWE that were 40% or greater at the lowest elevations, and little-to-no (-10 to +10%) changes to SWE at the highest elevations (e.g., Figure 3 and Figure 5). Between 15 April and 15 May, the pattern of 15 April SWE changes were shifted up in elevation by approximately 500 m (Figure S2), causing: 1) 15 May snow disappearance at elevations with 15 April projected SWE losses exceeding approximately 20%, 2) changes to 15 May SWE between -25% and -100% for many mid-elevation grid cells that experienced little-to-no decreases in 15 April SWE, and 3) little-to-no change in 15 May SWE at the highest-elevation grid cells in each domain (Figure 6). Put simply, datasets that exhibited sharper gradients in 15 April SWE changes with elevation resulted in larger changes between 15 April and 15 May SWE projections as these patterns were propagated up in elevation. This was also the case for the LOCA5, BCSD5, and MACA5 projections in the WY Rockies domain (Figure 6d), which had shaper gradients in SWE projections at elevations between 1500 and 2500 m (Figure S7 and Table S1). However, in all other domains, these projections exhibited more gradual changes to SWE projections with elevation (Figure 5, Figure S3, Figure S5, and Figure S9), resulting in a smaller change to SWE percent-difference between 15 April and 15 May as the climate change signal was propagated up in elevation. These results demonstrate hysteresis between snow projections on 15 April and 15 May, showing that the coherence between different snow projections in the snowmelt season is dependent on the coherence between models at the end-of-winter period. This is discussed more in Section 5.

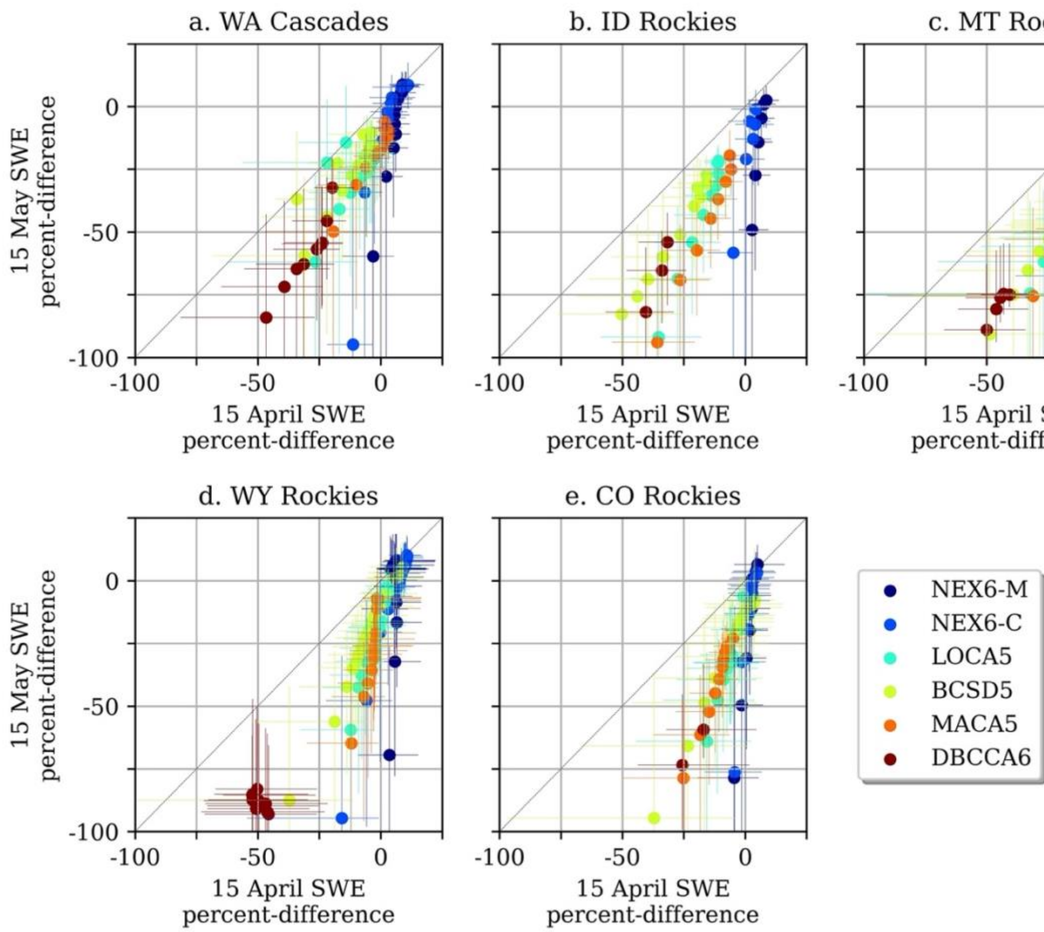

Figure 6. Projected changes to SWE for each dataset (colors) and domain (subplots) on 15 April (x-axis) and 15 May (y-axis). The median and interquartile range of projections over 100 m elevation bands are shown by the scatter points and whiskers, respectively. Plotted data only includes elevation bands where 15 May median SWE was greater than zero.

Disaggregating each projection's grid cells into a 0.01° grid resulted in smoother gradients to SWE percent-changes with elevation (e.g., Figure 5b). This approach also extrapolated SWE percent-change estimates to higher elevations that were sometimes unable to be represented by the coarser-scale snow projections. Overall, this extrapolation to higher elevations resulted in coarser-scale projections that increased in similarity with finer-scale snow projections. For example, in the ID Rockies domain, BCSD5 projections (1/8°) were unable to resolve grid cells at elevations of 2200 m or higher. At its highest native-resolution elevation band (2050 – 2150m), the BCSD5 dataset projected a 38% decrease to 15 May SWE, on average (Figure S4a).

However, preferentially sampling only those BCSD5 pixels that overlapped the highest elevation band captured by the 0.01° digital elevation model (2250 – 2350 m) only had a 27% decrease in 15 May SWE at the end-of-century period (Figure S4b). This SWE projection agreed closer with the LOCA5 (22% decrease) and MACA5 (20% decrease) estimates at the same elevations.

4.2. Snow classes with coherent snow projection patterns

As noted in Section 4.1, projected changes to end-of-century SWE exhibited similar patterns between the different snow projection datasets. While these patterns occurred at different elevations across each domain, these relationships could be used to identify regions with similar climate impacts and systematic differences across the projections. Using the NOS statistic as a metric for both climate change signals (Figure 2a) and the disparity across models (Figure 2b), six unique snow signals were classified. Of these six classes, five appeared in every domain, and appeared in the same sequence with increases in elevation. These snow classes, listed from lowest to highest elevations, included the following:

Class 1 (C1). Ephemeral snow cover: Different snow projections disagreed on the occurrence of 15 April snow in the first 20-year period (2016 – 2035), but end-of-century projections agreed that snow disappeared. This snow class covered the lowest-elevation portions of each domain.

C2. Seasonal snow line: This class included low-elevation and thin snowpack, but contained enough snow volume to calculate the overlap in SWE distributions between the early 21st century and end-of-century periods (Figure 2a), and the overlap between SWE projections across the different datasets (Figure 2b).

C3. SWE decreases > model disparity: This snow class had little overlap between SWE distributions rom the early 21st century and end-of-century periods. On average, differences in

SWE between the early 21st century and end-of-century periods exceeded the disparities across the SWE projections. In other words, the NOS for the climate change signal (Figure 2a) was smaller than the NOS for the model disparity (Figure 2b).

C4. Model disparity > changes to SWE: In this snow class, the differences across different snow projections were greater, on average, than the difference in SWE distributions between the early 21st century and end-of-century periods. These grid cells often had disagreements about the direction (positive or negative) of projected changes to SWE.

C5: SWE increases > model disparity: This class had projected increases to SWE with differences between the early 21st century and end-of-century SWE distributions that were larger, on average, than the difference in SWE projections across the different datasets.

C6: Elevations smoothed by coarser resolutions: The capability to resolve the highest peaks was limited by the spatial resolution of the projection datasets. This class represented elevation bands (calculated at 0.01° resolution) that couldn't be resolved by all snow projection datasets.

The grid cells that fell within each of the classes listed above were based on the climate change signals and model disparities calculated from the NOS statistic. In the WA Cascades domain (Figure 5c), elevations spanning 250 – 650 m had ephemeral snow and disagreements in snow extents between the projection datasets in the early 21st century (snow class C1). 15 April snow cover was more common for elevations between 650 – 1050 m, which had large projected decreases to end-of-century SWE, resulting in NOS statistics that could begin to resolve the disparity between models and the climate change signal (C2). At elevations just above this (1050 – 1550 m), SWE was projected to decrease by approximately 52%, on average, with relatively small variability across the snow projection datasets. This caused the early 21st century and end-of-century SWE distributions to separate to a degree that was larger than the disparity in SWE projections across different projection datasets (C3). Finally, the large spread and differing directions (positive/negative) of projected changes to SWE at elevations greater than 1550 m caused the disparity across models to exceed the average projected changes to SWE (C4). This included the highest-elevation grid cells (2150 m and higher) that were unable to be resolved by the coarser-resolution snow projections (C6).

Repeating the classifications from above in other domains (Figure S2 – S10), we could see that the snow classes appeared in each domain, but were shifted in elevation (Figure 7). For example, the snow classes in the nearby ID Rockies domain spanned elevation bands that were almost identical to those from the WA Cascades domain discussed above. However, the location of these snow classes was shifted up in elevation by approximately 400 m in the MT Rockies, 750 m in the WY Rockies, and 1550 m in the CO Rockies. Relative to 15 April, the 15 May snow line advanced up in elevation as snow extents were reduced from spring snowmelt in each domain, causing a growth in the elevations representing the first three snow classes (C1, C2, and C3), and a reduction to the elevations where the difference between snow projections exceeded the difference in SWE distributions between the early 21st century and end-of-century periods (C4) (Figure 7).

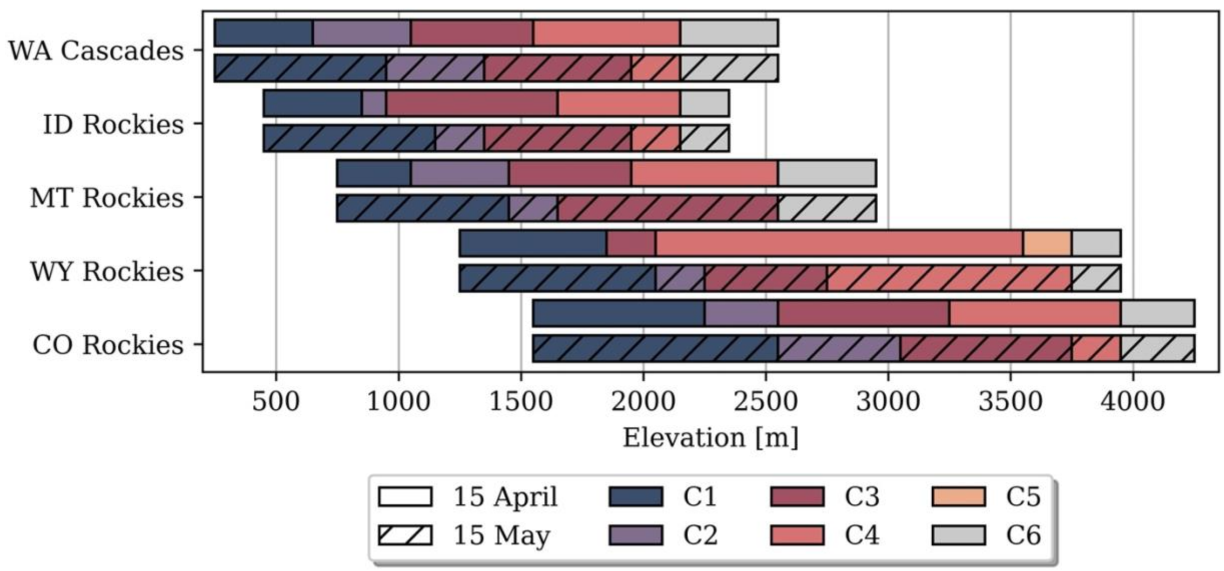

Figure 7. The elevations (x-axis) spanned by each snow class within each domain (y-axis) on 15 April (hollow) and 15 May (hatched).

Of the five domains investigated here, the SWE climate change signals in the WY Rockies domain were the most unique (Figure1, Figure S7, Figure S8, and Table 1). Notably, 15 April model disparities exceeded the SWE change signal (C4) for grid cells between approximately 2050 – 3550 m elevation, a span of elevations approximately 2.5 times larger than the C4 snow class in the other domains (Figure 7). This was likely driven by the winter climate in the interior WY Rockies, which was the coldest domain simulated here, and thereby had the smallest projected changes to 15 April end-of-century SWE on 15 April (Figure S7). However, the DBCCA6 data projected decreases to 15 April SWE that were as high as 52% across mid and high elevation grid cells (Figure 3). This is discussed more in Section 5. Despite the outlying projections from the DBCCA6 dataset, the WY Rockies domain was also the only domain to project SWE *increases* that were larger, on average, than the disparity across the models (Figure 7, C5). These grid cells were concentrated at elevations of 3550 – 3750m, although ensemble-median increases to 15 April SWE occurred at elevations as low as 2450 m for the NEX6-M projection dataset.

On 15 April, more than 90% of each domain's snow volume (e.g., Figure 5d) fell within classes where either the size of projected SWE decreases exceeded model disparities (C3) or model disparities exceeded projected changes to SWE (C4) (Figure 8a). Across the five domains, only in the ID Rockies domain did a majority (59%) of the domain's 15 April historical snow volume fall in regions where model disparities were smaller than the SWE climate change signal (C3). Despite containing a large portion of each domain's snow volume, the C4 snow class covered relatively small areal extents, covering only 22%, 9%, 10%, and 18% of the WA Cascades, ID Rockies, MT Rockies, and CO Rockies domains, respectively. As noted above, projections in the WY Rockies domain behaved differently, with 66% of the domain area and 93% of the domain's SWE volume exhibiting model disparities that were greater than the climate change signal. The proportion of the area and SWE volume that fell within each snow class on 15 April were largely flipped on 15 May (Figure S11), with a majority of snow volume (58 – 94%) existing in elevations where the climate change signal exceeded the model disparity. Again, the WY Rockies domain exhibited different patterns with 40% of the snow volume existing in the C3 class, and 58% existing in the C4 class, despite the C4 class only covering approximately 18% of the domain area.

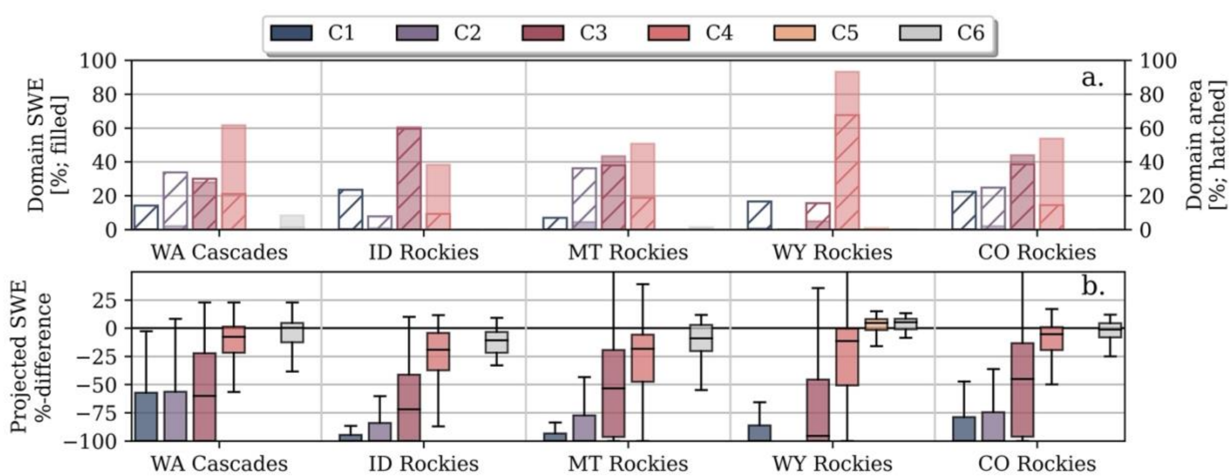

Figure 8. Bars show a) 15 April domain area (hatched) and SWE volume (filled) within each of the snow classes in each domain (x-axis). b) boxplots depict the distribution of all projected changes to 15 April SWE in each domain and snow class.

5. Discussion

The results in Section 4 compared 124 snow projections, including climate projections from two CMIP phases (CMIP5 and CMIP6), 58 GCMs, and six modeling approaches employing different downscaling approaches, downscaling reference datasets, spatial resolutions, and land surface models. Despite these differences, the snow projection datasets exhibited relationships with one another that had consistencies across each of the domains. For example, NEX6-M and NEX6-C snow projections had large changes in end-of-century SWE projections (approximately -13% per every 100 m decrease in elevation, on average) across 300 – 600 m spans in elevation. While this study does not investigate or attribute the sources of differences between snow projections, we hypothesize these sharp gradients in the SWE percent change signals were driven by the delta-method approach used by the NEX6-M and NEX6-C projections, which applied the same spatial maps of montly climate-change perturbations (Section 2.2), resulting in climate impacts on SWE projections that were far more localized in space than the other projection datasets. Despite this, NEX6-C projected larger decreases to end-of-century SWE than NEX6-M projections in each domain. This was driven by the low snow years (e.g., water years 1998, 2001, 2004, 2005, and 2009 in the WA Cascades) which had shallower low-elevation snow on 15 April, and increased sensitivity to increases in air temperature and melt energy.

SWE projections from the DBCCA6 dataset estimated significantly larger decreases to end-of-century 15 April SWE in each domain. This was particularly the case in the WY Rockies domain, where median SWE decreases exceeded 50% across all elevations, but a majority of the domain's snow volume resided in elevations where other snow projections estimated little-to-no change (-10% to +10%) (Figure S7). These outlying projections may have been driven by the downscaling procedure using the Daymet meteorological dataset (Thornton et al., 2021), which is relatively warmer than other reference meteorological datasets (Oyler et al., 2015). The DBCCA6 dataset also projected earlier dates of peak SWE, resulting in larger proportions of SWE melt prior to 15 April than the other projection datasets (Figure S12).

The relationship between elevation and 15 April projected changes to SWE were propagated into the 15 May snow projections in each domain and projection dataset (Figure 6). In fact, the elevational pattern of 15 May projected changes to SWE could be reconstructed by 1) shifting the 15 April SWE projections up in elevation, and 2) adding increases to spring snowmelt, which were larger at lower elevations, but decreased with elevation. On average, across the five domains, the spatial Pearson Correlation Coefficient between 15 April and 15 May SWE projections (Figure 6) was 0.82 for the NEX6-M projections (on average, across the 5 domains), 0.96 for the NEX6-C projections, 0.92 for the LOCA5 projections, 0.96 for the BCSD5 projections, 0.97 for the MACA5 projections, and 0.88 for the DBCCA6 projections. As discussed in Section 4.1, the slope of the relationship between the 15 April and 15 May SWE projections was most influenced by the elevational pattern of 15 April SWE projections. For example, 15 April SWE projections in the WY Rockies domain exhibited sharper gradients with elevation (Figure S7). When this SWE projection pattern was shifted up in elevation on 15 May (Figure S8), many grid cells with little-to-no 15 April SWE losses exhibited losses of 25% or greater on 15 May, causing a more dramatic slope in the relationship between 15 April and 15 May SWE projections in this domain, relative to other domains (Figure 6).

The consistent patterns between the different snow projections, and the hysteresis in these patterns over time, suggested that the coherent relationships between the snow projections can be used to identify classes where and when 1) disparate approaches converge to common projections of future change, and 2) improvements in systematic projection disparities could provide the greatest improvement in projections of future snow water resources. In Section 4, we chose to classify these snow classes using the NOS statistic (Equation 3), which benchmarked the disparities across snow projection datasets versus the underlying climate change signals. To our knowledge, this type of approach has not been used in other studies. However, we found that the NOS statistic had multiple benefits. First, this approach relied on U-values from the Mann-Whitney non-parametric ranked sum test, which standardized the overlap between two datasets by the number of samples in each (Equations 1 and 2, n_1 and n_2). Relative to more common measurements (e.g., percentiles of overlap and ANOVA analyses) NOS provided a continuous normalized statistic ranging between 0.0 and 0.5 that was less-sensitive to comparisons between projections with different numbers of GCMs. Additionally, SWE projections across 100 m elevation bands did not consistently conform to any theoretical distribution (e.g, normal, lognormal, chi, etc.), indicating that a statistic based on a non-parametric test, such as the Mann-Whitney U, would perform best.

Much like the projected changes to end-of-century SWE, the distribution of the NOS statistic for 15 April climate change signals (Figure 2a) and model disparities (Figure 2b) followed similar patterns with increases in elevation across the modeling domains (Figure 5c, Figure S3c, Figure S5c, Figure S7c, Figure S9c). This resulted in the similar, but elevation-shifted distribution of snow classes (C1 – C6) shown in Figure 7. Overall, the climate change signal varied with elevation more than the projection disparity. For example, in the WA Cascades domain on 15 April (Figure 5c), the standard deviation of the NOS statistic for the climate change signal was 49% larger than the standard deviation of the NOS for model disparities. In this same domain, the distributions of NOS for the climate change and model disparity signals were approximately equal at an elevation of 1550 m (Figure 5c). This inflection point represented the location where snow losses projected at lower elevations (C1 – C3, 250 – 1550 m) were in agreement in sign (positive/negative) and of similar magnitudes, but the disparity across models exceeded the climate change signal at higher elevations (C4). For the 124 snow projections tested here, the median projected change to 15 April SWE at this inflection point was approximately -26% in the WA Cascades (Figure 8). For the other domains, these inflection points occurred at: 1650 m elevation and -48% projected changes to SWE in the ID Rockies, 1950 m and -44% in the MT Rockies, 2250 m and -35% in the WY Rockies, and 2750 m and -23% in the CO Rockies.

Based on the inflection points above, grid cells with 15 April ensemble-average projected decreases to SWE of 48% or greater (Figure 3) were among the highest-confidence climate change signals. Siirila-Woodburn et al. (2021) suggested that end-of-winter projected SWE losses of 48% or greater are likely for the vast majority of Western US by the end of the century. However, disproportionate amounts of annual Western US streamflow come from high-elevation montane regions which cover only small portions of the Western US land mass (Li et al., 2017), and are subject to some of the highest snow projection uncertainties. In this study, Figure 8a shows that snow classes with higher-confidence projected SWE decreases (snow classes C1 – C3) account for more than half of the area of the WA Cascades, ID Rockies, MT Rockies, and CO Rockies domains. Yet, these areas contain less than 63%, and as little as 6%, of each domain's historical snow volume. In other words, while projections employing disparate modeling approaches agree across large spatial extents, the locations with disagreements contain disproportionate amounts of snow. This issue was particularly prevalent in the WY Rockies domain where only 5% and 1% of the historical snow volume had higher-confidence SWE decreases (C1 – C3) and SWE increases (C5), respectively.

We found that 15 April model disparity measured using the NOS statistic (Figure 2b) was at it's worst for elevations approximately 250 m higher than the inflection points. In these elevations, SWE projections from the NEX6-M and NEX6-C SWE datasets tended to diverge from the LOCA5, BCSD5, and MACA5 projections, approaching smaller end-of-century SWE change estimates. This was opposed to SWE projections for the DBCCA6 dataset, which estimated larger SWE losses than any other dataset for elevations both in this span of elevations, and at all higher elevations. Although limited in area, this 250 m elevation band contained significant amounts of SWE volume (Figure 9), accounting for 27% of the historical snow volume in the WA Cascades, 31% in the ID Rockies, 33% in the MT Rockies, 11% in the WY Rockies, and 26% in the CO Rockies.

Based on Figure 9, and the snow projection datasets compared in this study, we expect that the greatest improvements to the coherence of snow projections could come from investigating and attributing the sources of projection disparities in the 250 m elevation bands above the inflection points. However, we recognize that improving the coherence of snow projections in these regions is challenging. For example, for the domains investigated here, the average terrain slope in the 250 m elevation bands above the inflection point is approximately 14º. This means that for a conservative and steadily-inceasing slope, elevation increases approximately 249 m for every 1000 m in horizontal distance. Assuming common air temperature lapse rates (e.g., Arsenault et al., 2018; Minder et al., 2010), air temperature within a 100 km GCM grid cell with these characteristics vary consistently by as much as 8º C, and often more. This highlights the challenges with modeling meteorological conditions at at scales significantly smaller than the spatial resolutions of GCMs, especially considering fine-scale processes like mountain pass air mixing and snow albedo feedbacks. Grid cells within these 250 m elevation bands are also often in inaccessible, hazardous, and unmonitored terrain. In fact, the 250 m elevation band of focus in the CO Rockies domain falls at approximately 3250 – 3500 m in elevation, which is higher than approximately 95% of Snow Telemetry (SNOTEL) stations in the Western United States, making it difficult to validate GCMs and reference downscaling datasets. Fortunately, since disparities across snow projections demonstrated repeatable, but elevation-shifted patterns in each domain, we hypothesize that improvements to projection disparities in one domain may translate to improvements in other domains. In other words, while the cause of disparities between models may be difficult to diagnose in this high elevation region in the CO Rockies, the pattern of disparities between projections in this regions was similar to the pattern of disparities at more-accessible and observed elevations between 1550 and 1800 m in the WA Cascades. This hypothesis is beyond the scope of this manuscript, and will be investigated by future research.

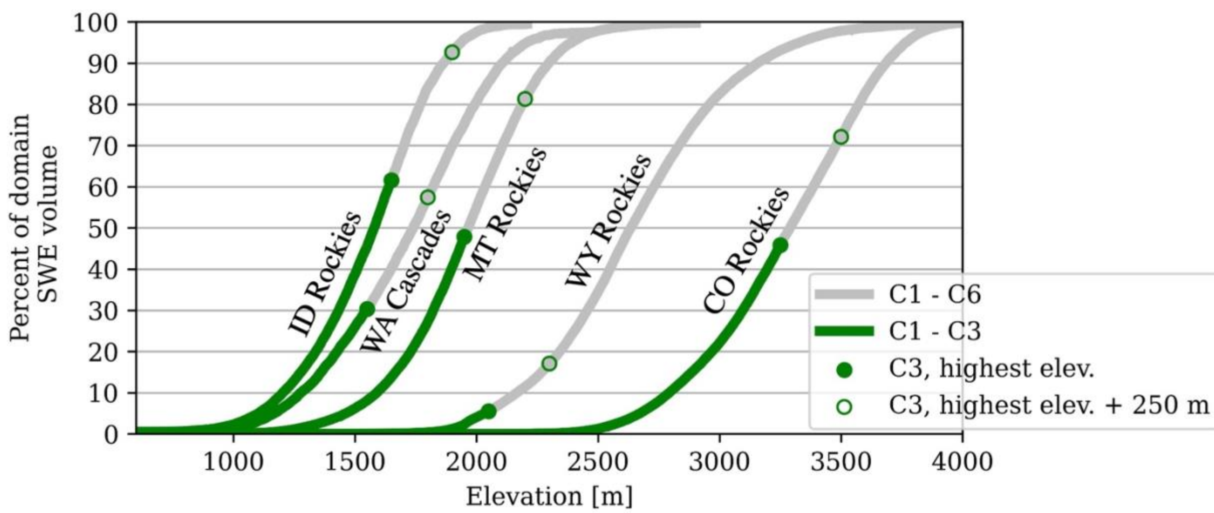

Figure 9. Historical SWE distribution in each domain for all snow classes (gray), and snow classes with the most-coherent decreases to end-of-century SWE (green). The difference between the filled and hollow scatter points show the difference in SWE volume over a 250 m elevation band above the elevation at which model disparity first equals the climate change signal.

Our results show that benchmarking ensembles of snow projection climate change signals using the disparity across models can provide a path forward for identifying coherence between projections, both in terms of identifying locations where disparate modeling methodologies approach common results, and identifying systematic and repeatable departures between snow projection datasets. We acknowledge that the results presented here were dependent on the six snow projections used, and the two analogous emissions scenarios (SSP 2-4.5 and RCP 4.5). Therefore, future research should continue on this approach, adding more snow projections including a range of climate forcing and modeling approaches. Given the continued development of state-of-the-art climate models, meteorological downscaling approaches, and land surface models, we expect large-ensemble approaches like the approaches used here to be valuable for identifying and communicating the high-confidence changes to future snow water resources and the resulting impacts on the land surface hydrology, and identifying the regions where our estimates of future snowpack may benefit most from further research and development.

6. Conclusions

Differences in modeling approaches such as different land surface models, climate models, downscaling approaches, and spatial resolutions can cause cascading differences in model forcing and simulated snow evolution, making it difficult to determine the most accurate projections, and the causes of disparities between different projection datasets. This is particularly the case in mountainous terrain, where the sparsity of observations and fine-scale spatial variabilities in meteorological conditions make climate and snow projections challenging.

Here, we found that projected changes to end-of-century SWE, climate change signals, and model disparities showed relationships with terrain elevation in five Western US montane domains. Using these relationships, we were able to partition each domain into snow classes that exhibited similar relationships, but were shifted in elevation (Figure 7). The lowest elevations of each domain exhibited high-confidence projected decreases to 15 April SWE that were larger in magnitude than the disparity across the models (Figure 3 and Figure 5). Across the five domains, 15 April projections agreed in regions where median projected decreases to end-of-century SWE were 48% or larger. However, some regions like the Colorado Rockies and Washington Cascades had better coherence across the projections, resulting in decreases to end-of-century SWE with high levels of agreement between snow projections at grid cells experiencing more than 23% and 26% decreases, respectively. Grid cells with high-confidence SWE projections covered a majority of the domain area in the Washington Cascades, Idaho Rockies, Montana Rockies, and Colorado Rockies (Figure 8). Despite this, a majority of annual SWE volume existed in higher elevation regions where the disparities between snow projections exceeded the projected changes to SWE. This was particularly the case in the Wyoming Rockies domain, where colder climates resulted in significantly smaller projected changes to 15 April SWE (Figure 3). In fact, only this domain experienced grid cells with projected high-confidence *increases* to end-of-century SWE. However, this only occurred over a small span of elevations (3550 – 3750 m), accounting for approximately 1% of this domain's total area, and less than 1% of the total SWE volume. In summary, we found that despite the widespread agreement in snow projections spatially, the greatest disagreements between projections occurred in the regions with the greatest snow volumes, emphasizing the need to improve snow projection coherence in high-elevation terrain.

Results also found strong relationships ($r \geq 0.82$) between 15 April and 15 May SWE projections for each snow projection dataset in each domain (Figure 6). In fact, 15 May SWE projections could be reproduced by shifting the 15 April SWE projections up in elevation, and enhancing the snowmelt that occurred for thinner snowpacks in warmer future climates. This suggested that improvements to the spread and certainty of 15 April SWE projections would translate to improvements between the projections at later dates. These results suggest that future studies should consider the use of large-ensemble approaches, like the approach used here, with additional snow projection datasets and future emissions scenarios, as a basis for 1) identifying and communicating the highest-confidence changes to future snow water resources, and 2) the locations and periods where work should focus most on honing future projection datasets.

Acknowledgements

This work was supported in part by funding from the National Aeronautics and Space Administration (NASA) Terrestrial Hydrology Program. Computing was supported by the NASA Center for Climate Simulation (NCCS) and the Oak Ridge Leadership Computing Facility at Oak Ridge National Laboratory, which is a Department of Energy Office of Science User Facility. The authors would also like to acknowledge support from the US Geological Survey (grant no. G21AC10645), in addition to insight and advice provided by the US Fish and Wildlife Service and Dr. Stefan Rahimi. The authors declare that they have no conflict of interest.

Data Availability Statement

The Western United States SWE reanalysis can be accessed through the National Snow and Ice Data Center (Fang and Margulis, 2020). BCSD5 and LOCA5 (Table 1) projections can be accessed from Maurer et al. (2007). MACA5 data can be accessed from the Northwest Knowledge Network (Abatzoglou et al., 2014). DBCCA6 projections can be accessed from Kao et al. (2022b). Finally, the novel dataset generated for this project can be accessed through the NASA NCCS data portal, this includes the NEX-GDDP-CMIP6 climate forcing (https://ds.nccs.nasa.gov/thredds/catalog/AMES/NEX/GDDP-CMIP6/catalog.html), and the NEX6-M and NEX-C snow simulation outputs (https://portal.nccs.nasa.gov/lisdata_pub/FWS/). The authors are actively working on providing the NEX6-M and NEX6-C snow projections to persistent and doi-citable data repositories.

References

Aas, K.S., Gisnås, K., Westermann, S., Berntsen, T.K., 2017. A Tiling Approach to Represent Subgrid Snow Variability in Coupled Land Surface–Atmosphere Models. J. Hydrometeor. 18, 49–63. https://doi.org/10.1175/JHM-D-16-0026.1

Abatzoglou, J., Hegewisch, K., Hegewisch, K., Hegewisch, K., 2014. MACAv2-LIVNEH: Gridded Daily Statistical Downscaling of CMIP5 using LIVNEH training dataset. USGS ScienceBase.

Abatzoglou, J.T., Brown, T.J., 2012. A comparison of statistical downscaling methods suited for wildfire applications. International Journal of Climatology 32, 772–780. https://doi.org/10.1002/joc.2312

Alder, J.R., Hostetler, S.W., 2019. The Dependence of Hydroclimate Projections in Snow-Dominated Regions of the Western United States on the Choice of Statistically Downscaled Climate Data. Water Resources Research 55, 2279–2300. https://doi.org/10.1029/2018WR023458

Arsenault, K.R., Kumar, S.V., Geiger, J.V., Wang, S., Kemp, E., Mocko, D.M., Beaudoing, H.K., Getirana, A., Navari, M., Li, B., Jacob, J., Wegiel, J., Peters-Lidard, C.D., 2018. The Land surface Data Toolkit (LDT v7.2) – a data fusion environment for land data assimilation systems. Geoscientific Model Development 11, 3605–3621. https://doi.org/10.5194/gmd-11-3605-2018

Barnett, T.P., Adam, J.C., Lettenmaier, D.P., 2005. Potential impacts of a warming climate on water availability in snow-dominated regions. Nature 438, 303. https://doi.org/10.1038/nature04141

Barsugli, J.J., Ray, A.J., Livneh, B., Dewes, C.F., Heldmyer, A., Rangwala, I., Guinotte, J.M., Torbit, S., 2020. Projections of Mountain Snowpack Loss for Wolverine Denning Elevations in the Rocky Mountains. Earth's Future 8, e2020EF001537. https://doi.org/10.1029/2020EF001537

Brekke, L., Thrasher, B.L., Maurer, E.P., Pruitt, T., 2013. Downscaled CMIP3 and CMIP5 Climate and Hydrology Projections: Release of Downscaled CMIP5 Climate Projections, Comparison with Preceding Information, and Summary of User Needs. US Bureau of Reclamation.

Chegwidden, O.S., Nijssen, B., Rupp, D.E., Arnold, J.R., Clark, M.P., Hamman, J.J., Kao, S.-C., Mao, Y., Mizukami, N., Mote, P.W., Pan, M., Pytlak, E., Xiao, M., 2019. How Do Modeling Decisions Affect the Spread Among Hydrologic Climate Change Projections? Exploring a Large Ensemble of Simulations Across a Diversity of Hydroclimates. Earth's Future 7, 623–637. https://doi.org/10.1029/2018EF001047

Clark, M.P., Hendrikx, J., Slater, A.G., Kavetski, D., Anderson, B., Cullen, N.J., Kerr, T., Hreinsson, E.Ö., Woods, R.A., 2011. Representing spatial variability of snow water equivalent in hydrologic and land-surface models: A review. Water Resources Research 47. https://doi.org/10.1029/2011WR010745

Currier, W.R., Thorson, T., Lundquist, J.D., 2017. Independent Evaluation of Frozen Precipitation from WRF and PRISM in the Olympic Mountains. J. Hydrometeor. 18, 2681–2703. https://doi.org/10.1175/JHM-D-17-0026.1

Essery, R., Morin, S., Lejeune, Y., B Ménard, C., 2013. A comparison of 1701 snow models using observations from an alpine site. Advances in Water Resources, Snow–Atmosphere Interactions and Hydrological Consequences 55, 131–148. https://doi.org/10.1016/j.advwatres.2012.07.013

Eyring, V., Bony, S., Meehl, G.A., Senior, C.A., Stevens, B., Stouffer, R.J., Taylor, K.E., 2016. Overview of the Coupled Model Intercomparison Project Phase 6 (CMIP6) experimental design and organization. Geoscientific Model Development 9, 1937–1958. https://doi.org/10.5194/gmd-9-1937-2016

Fang, Y., Liu, Y., Margulis, S.A., 2022. A western United States snow reanalysis dataset over the Landsat era from water years 1985 to 2021. Sci Data 9, 677. https://doi.org/10.1038/s41597-022-01768-7

Fang, Y., Liu, Y., Margulis, S.A., 2020. A New Landsat-era Snow Reanalysis Dataset over the Western United States 2020, C047-0017.

Fang, Y., Margulis, S.A., 2020. Western United States UCLA Daily Snow Reanalysis, Version 1 [WWW Document]. National Snow and Ice Data Center Distributed Active Archive Center. URL https://doi.org/10.5067/PP7T2GBI52I2 (accessed 7.28.23).

Fyfe, J.C., Derksen, C., Mudryk, L., Flato, G.M., Santer, B.D., Swart, N.C., Molotch, N.P., Zhang, X., Wan, H., Arora, V.K., Scinocca, J., Jiao, Y., 2017. Large near-term projected snowpack loss over the western United States. Nat Commun 8, 14996. https://doi.org/10.1038/ncomms14996

Gelaro, R., McCarty, W., Suárez, M.J., Todling, R., Molod, A., Takacs, L., Randles, C.A., Darmenov, A., Bosilovich, M.G., Reichle, R., Wargan, K., Coy, L., Cullather, R., Draper, C., Akella, S., Buchard, V., Conaty, A., Silva, A.M. da, Gu, W., Kim, G.-K., Koster, R., Lucchesi, R., Merkova, D., Nielsen, J.E., Partyka, G., Pawson, S., Putman, W., Rienecker, M., Schubert, S.D., Sienkiewicz, M., Zhao, B., 2017. The Modern-Era Retrospective Analysis for Research and Applications, Version 2 (MERRA-2). Journal of Climate 30, 5419–5454. https://doi.org/10.1175/JCLI-D-16-0758.1

Gergel, D.R., Nijssen, B., Abatzoglou, J.T., Lettenmaier, D.P., Stumbaugh, M.R., 2017. Effects of climate change on snowpack and fire potential in the western USA. Climatic Change 141, 287–299.

Ghan, S.J., Shippert, T., 2006. Physically Based Global Downscaling: Climate Change Projections for a Full Century. Journal of Climate 19, 1589–1604. https://doi.org/10.1175/JCLI3701.1

Guan, B., Waliser, D.E., Ralph, F.M., Fetzer, E.J., Neiman, P.J., 2016. Hydrometeorological characteristics of rain-on-snow events associated with atmospheric rivers. Geophysical Research Letters 43, 2964–2973. https://doi.org/10.1002/2016GL067978

Gutmann, E., Pruitt, T., Clark, M.P., Brekke, L., Arnold, J.R., Raff, D.A., Rasmussen, R.M., 2014. An intercomparison of statistical downscaling methods used for water resource assessments in the United States. Water Resources Research 50, 7167–7186. https://doi.org/10.1002/2014WR015559

Gutmann, E.D., Rasmussen, R.M., Liu, C., Ikeda, K., Gochis, D.J., Clark, M.P., Dudhia, J., Thompson, G., 2012. A Comparison of Statistical and Dynamical Downscaling of Winter Precipitation over Complex Terrain. J. Climate 25, 262–281. https://doi.org/10.1175/2011JCLI4109.1

Hale, K.E., Wlostowski, A.N., Badger, A.M., Musselman, K.N., Livneh, B., Molotch, N.P., 2022. Modeling streamflow sensitivity to climate warming and surface water inputs in a montane catchment. Journal of Hydrology: Regional Studies 39, 100976. https://doi.org/10.1016/j.ejrh.2021.100976

Hamlet, A.F., Mote, P.W., Clark, M.P., Lettenmaier, D.P., 2007. Twentieth-Century Trends in Runoff, Evapotranspiration, and Soil Moisture in the Western United States*. Journal of Climate 20, 1468–1486. https://doi.org/10.1175/JCLI4051.1

Harpold, A., Brooks, P., Rajagopal, S., Heidbuchel, I., Jardine, A., Stielstra, C., 2012. Changes in snowpack accumulation and ablation in the intermountain west. Water Resources Research 48. https://doi.org/10.1029/2012WR011949

Harpold, A.A., Brooks, P.D., 2018. Humidity determines snowpack ablation under a warming climate. Proceedings of the National Academy of Sciences 115, 1215–1220. https://doi.org/10.1073/pnas.1716789115

Hawkins, E., Sutton, R., 2009. The Potential to Narrow Uncertainty in Regional Climate Predictions. Bulletin of the American Meteorological Society 90, 1095–1108. https://doi.org/10.1175/2009BAMS2607.1

Hidalgo, H.G., Dettinger, M.D., Cayan, D.R., 2008. Downscaling with constructed analogues: Daily precipitation and temperature fields over the United States. California Energy Commission PIER Final Project Report CEC-500-2007-123.

Hughes, M., Hall, A., Fovell, R.G., 2009. Blocking in Areas of Complex Topography, and Its Influence on Rainfall Distribution. Journal of the Atmospheric Sciences 66, 508–518. https://doi.org/10.1175/2008JAS2689.1

Hughes, M., Lundquist, J.D., Henn, B., 2017. Dynamical downscaling improves upon gridded precipitation products in the Sierra Nevada, California. Clim Dyn. https://doi.org/10.1007/s00382-017-3631-z

Ikeda, K., Rasmussen, R., Liu, C., Newman, A., Chen, F., Barlage, M., Gutmann, E., Dudhia, J., Dai, A., Luce, C., Musselman, K., 2021. Snowfall and snowpack in the Western U.S. as captured by convection permitting climate simulations: current climate and pseudo global warming future climate. Clim Dyn 57, 2191–2215. https://doi.org/10.1007/s00382-021-05805-w

IPCC, 2021. Climate change 2021: The physical science basis. Contribution of Working Group I to the sixth assessement report of the Intergovernnmental Panel on Climate Change [Masson-Delmotte, V., P. Zhai, A. Pirani, S.L. Connors, C. Péan, S. Berger, N. Caud, Y. Chen, L. Goldfarb, M.I. Gomis, M. Huang, K. Leitzell, E. Lonnoy, J.B.R. Matthews, T.K. Maycock, T. Waterfield, O. Yelekçi, R. Yu, and B. Zhou (eds.)]. Cambridge University Press, Cambridge, U.K., and New York, NY, USA.

Jennings, K.S., Winchell, T.S., Livneh, B., Molotch, N.P., 2018. Spatial variation of the rain–snow temperature threshold across the Northern Hemisphere. Nat Commun 9, 1148. https://doi.org/10.1038/s41467-018-03629-7

Kao, S.-C., Ashfaq, M., Rastogi, D., Gangrade, S., Uria Martinez, R., Fernandez, A., Konapala, G., Voisin, N., Zhou, T., Xu, W., Gao, H., Zhao, B., Zhao, G., 2022a. The Third Assessment of the Effects of Climate Change on Federal Hydropower (No. ORNL/TM-

2021/2278). Oak Ridge National Lab. (ORNL), Oak Ridge, TN (United States). https://doi.org/10.2172/1887712

Kao, S.-C., Moetasim, A., Deeksha, R., Gangrade, S., 2022b. CMIP6-based Multi-model Hydroclimate Projection over the Conterminous US. HydroSource. https://doi.org/10.21951/SWA9505V3/1887469

Kapnick, S., Hall, A., 2012. Causes of recent changes in western North American snowpack. Clim Dyn 38, 1885–1899. https://doi.org/10.1007/s00382-011-1089-y

Kim, R.S., Kumar, S., Vuyovich, C., Houser, P., Lundquist, J., Mudryk, L., Durand, M., Barros, A., Kim, E.J., Forman, B.A., Gutmann, E.D., Wrzesien, M.L., Garnaud, C., Sandells, M., Marshall, H.-P., Cristea, N., Pflug, J.M., Johnston, J., Cao, Y., Mocko, D., Wang, S., 2021. Snow Ensemble Uncertainty Project (SEUP): quantification of snow water equivalent uncertainty across North America via ensemble land surface modeling. The Cryosphere 15, 771–791. https://doi.org/10.5194/tc-15-771-2021

Koster, R.D., Mahanama, S.P.P., Livneh, B., Lettenmaier, D.P., Reichle, R.H., 2010. Skill in streamflow forecasts derived from large-scale estimates of soil moisture and snow. Nature Geosci 3, 613–616. https://doi.org/10.1038/ngeo944

Krinner, G., Derksen, C., Essery, R., Flanner, M., Hagemann, S., Clark, M., Hall, A., Rott, H., Brutel-Vuilmet, C., Kim, H., Ménard, C.B., Mudryk, L., Thackeray, C., Wang, L., Arduini, G., Balsamo, G., Bartlett, P., Boike, J., Boone, A., Chéruy, F., Colin, J., Cuntz, M., Dai, Y., Decharme, B., Derry, J., Ducharne, A., Dutra, E., Fang, X., Fierz, C., Ghattas, J., Gusev, Y., Haverd, V., Kontu, A., Lafaysse, M., Law, R., Lawrence, D., Li, W., Marke, T., Marks, D., Ménégoz, M., Nasonova, O., Nitta, T., Niwano, M., Pomeroy, J., Raleigh, M.S., Schaedler, G., Semenov, V., Smirnova, T.G., Stacke, T., Strasser, U., Svenson, S., Turkov, D., Wang, T., Wever, N., Yuan, H., Zhou, W., Zhu, D., 2018. ESM-SnowMIP: assessing snow models and quantifying snow-related climate feedbacks. Geoscientific Model Development 11, 5027–5049. https://doi.org/10.5194/gmd-11-5027-2018

Le Roux, R., Katurji, M., Zawar-Reza, P., Quénol, H., Sturman, A., 2018. Comparison of statistical and dynamical downscaling results from the WRF model. Environmental Modelling & Software 100, 67–73. https://doi.org/10.1016/j.envsoft.2017.11.002

Lehner, F., Deser, C., Maher, N., Marotzke, J., Fischer, E.M., Brunner, L., Knutti, R., Hawkins, E., 2020. Partitioning climate projection uncertainty with multiple large ensembles and CMIP5/6. Earth System Dynamics 11, 491–508. https://doi.org/10.5194/esd-11-491-2020

Leung, L.R., Qian, Y., Bian, X., Washington, W.M., Han, J., Roads, J.O., 2004. Mid-Century Ensemble Regional Climate Change Scenarios for the Western United States. Climatic Change 62, 75–113. https://doi.org/10.1023/B:CLIM.0000013692.50640.55

Li, D., Wrzesien, M.L., Durand, M., Adam, J., Lettenmaier, D.P., 2017. How much runoff originates as snow in the western United States, and how will that change in the future? Geophysical Research Letters 44, 6163–6172. https://doi.org/10.1002/2017GL073551

López-Moreno, J.I., Gascoin, S., Herrero, J., Sproles, E.A., Pons, M., Alonso-González, E., Hanich, L., Boudhar, A., Musselman, K.N., Molotch, N.P., Sickman, J., Pomeroy, J., 2017. Different sensitivities of snowpacks to warming in Mediterranean climate mountain areas. Environ. Res. Lett. 12, 074006. https://doi.org/10.1088/1748-9326/aa70cb

Lumbrazo, C., Bennett, A., Currier, W.R., Nijssen, B., Lundquist, J., 2022. Evaluating Multiple Canopy-Snow Unloading Parameterizations in SUMMA With Time-Lapse Photography

Characterized by Citizen Scientists. Water Resources Research 58, e2021WR030852. https://doi.org/10.1029/2021WR030852

Lundquist, J.D., Hughes, M., Henn, B., Gutmann, E.D., Livneh, B., Dozier, J., Neiman, P., 2015. High-Elevation Precipitation Patterns: Using Snow Measurements to Assess Daily Gridded Datasets across the Sierra Nevada, California. J. Hydrometeor. 16, 1773–1792. https://doi.org/10.1175/JHM-D-15-0019.1

Lundquist, J.D., Minder, J.R., Neiman, P.J., Sukovich, E., 2010. Relationships between Barrier Jet Heights, Orographic Precipitation Gradients, and Streamflow in the Northern Sierra Nevada. Journal of Hydrometeorology 11, 1141–1156. https://doi.org/10.1175/2010JHM1264.1

Maurer, E.P., Brekke, L., Pruitt, T., Duffy, P.B., 2007. Fine-resolution climate change projections enhance regional climate change impact studies. Eos, Transactions, American Geophysical Union 88, 504. https://doi.org/doi:10.1029/2007EO470006

McCrary, R.R., Mearns, L.O., 2019. Quantifying and Diagnosing Sources of Uncertainty in Midcentury Changes in North American Snowpack from NARCCAP. Journal of Hydrometeorology 20, 2229–2252. https://doi.org/10.1175/JHM-D-18-0248.1

Minder, J.R., Letcher, T.W., Skiles, S.M., 2016. An evaluation of high-resolution regional climate model simulations of snow cover and albedo over the Rocky Mountains, with implications for the simulated snow-albedo feedback. Journal of Geophysical Research: Atmospheres 121, 9069–9088. https://doi.org/10.1002/2016JD024995

Minder, J.R., Mote, P.W., Lundquist, J.D., 2010. Surface temperature lapse rates over complex terrain: Lessons from the Cascade Mountains. Journal of Geophysical Research: Atmospheres 115. https://doi.org/10.1029/2009JD013493

Mote, P.W., Li, S., Lettenmaier, D.P., Xiao, M., Engel, R., 2018. Dramatic declines in snowpack in the western US. npj Clim Atmos Sci 1, 1–6. https://doi.org/10.1038/s41612-018-0012-1

Mudryk, L.R., Derksen, C., Kushner, P.J., Brown, R., 2015. Characterization of Northern Hemisphere Snow Water Equivalent Datasets, 1981–2010. Journal of Climate 28, 8037–8051. https://doi.org/10.1175/JCLI-D-15-0229.1

Musselman, K.N., Addor, N., Vano, J.A., Molotch, N.P., 2021. Winter melt trends portend widespread declines in snow water resources. Nat. Clim. Chang. 11, 418–424. https://doi.org/10.1038/s41558-021-01014-9

Musselman, K.N., Clark, M.P., Liu, C., Ikeda, K., Rasmussen, R., 2017. Slower snowmelt in a warmer world. Nature Clim Change 7, 214–219. https://doi.org/10.1038/nclimate3225

Orlowsky, B., Bothe, O., Fraedrich, K., Gerstengarbe, F.-W., Zhu, X., 2010. Future Climates from Bias-Bootstrapped Weather Analogs: An Application to the Yangtze River Basin. Journal of Climate 23, 3509–3524. https://doi.org/10.1175/2010JCLI3271.1

Oyler, J.W., Dobrowski, S.Z., Ballantyne, A.P., Klene, A.E., Running, S.W., 2015. Artificial amplification of warming trends across the mountains of the western United States. Geophysical Research Letters 42, 153–161. https://doi.org/10.1002/2014GL062803

Pflug, J.M., Liston, G.E., Nijssen, B., Lundquist, J.D., 2019. Testing Model Representations of Snowpack Liquid Water Percolation Across Multiple Climates. Water Resources Research 55, 4820–4838. https://doi.org/10.1029/2018WR024632

Pflug, J.M., Margulis, S.A., Lundquist, J.D., 2022. Inferring watershed-scale mean snowfall magnitude and distribution using multidecadal snow reanalysis patterns and snow pillow observations. Hydrological Processes 36, e14581.

Pierce, D.W., Cayan, D.R., Thrasher, B.L., 2014. Statistical Downscaling Using Localized Constructed Analogs (LOCA). Journal of Hydrometeorology 15, 2558–2585. https://doi.org/10.1175/JHM-D-14-0082.1

Qian, Y., Ghan, S.J., Leung, L.R., 2010. Downscaling hydroclimatic changes over the Western US based on CAM subgrid scheme and WRF regional climate simulations. International Journal of Climatology 30, 675–693. https://doi.org/10.1002/joc.1928

Raleigh, M.S., Lundquist, J.D., Clark, M.P., 2015. Exploring the impact of forcing error characteristics on physically based snow simulations within a global sensitivity analysis framework. Hydrol. Earth Syst. Sci. 19, 3153–3179. https://doi.org/10.5194/hess-19-3153-2015

Rasmussen, R., Ikeda, K., Liu, C., Gochis, D., Clark, M., Dai, A., Gutmann, E., Dudhia, J., Chen, F., Barlage, M., Yates, D., Zhang, G., 2014. Climate Change Impacts on the Water Balance of the Colorado Headwaters: High-Resolution Regional Climate Model Simulations. Journal of Hydrometeorology 15, 1091–1116. https://doi.org/10.1175/JHM-D-13-0118.1

Ray, P., Wi, S., Schwarz, A., Correa, M., He, M., Brown, C., 2020. Vulnerability and risk: climate change and water supply from California's Central Valley water system. Climatic Change 161, 177–199. https://doi.org/10.1007/s10584-020-02655-z

Reynolds, D.S., Pflug, J.M., Lundquist, J.D., 2021. Evaluating Wind Fields for Use in Basin-Scale Distributed Snow Models. Water Resources Research 57, e2020WR028536. https://doi.org/10.1029/2020WR028536

Rhoades, A.M., Jones, A.D., Ullrich, P.A., 2018a. The Changing Character of the California Sierra Nevada as a Natural Reservoir. Geophysical Research Letters 45, 13,008-13,019. https://doi.org/10.1029/2018GL080308

Rhoades, A.M., Ullrich, P.A., Zarzycki, C.M., 2018b. Projecting 21st century snowpack trends in western USA mountains using variable-resolution CESM. Clim Dyn 50, 261–288. https://doi.org/10.1007/s00382-017-3606-0

Sheffield, J., Goteti, G., Wood, E.F., 2006. Development of a 50-Year High-Resolution Global Dataset of Meteorological Forcings for Land Surface Modeling. Journal of Climate 19, 3088–3111. https://doi.org/10.1175/JCLI3790.1

Siirila-Woodburn, E.R., Rhoades, A.M., Hatchett, B.J., Huning, L.S., Szinai, J., Tague, C., Nico, P.S., Feldman, D.R., Jones, A.D., Collins, W.D., 2021. A low-to-no snow future and its impacts on water resources in the western United States. Nature Reviews Earth & Environment 2, 800–819.

Sofaer, H.R., Barsugli, J.J., Jarnevich, C.S., Abatzoglou, J.T., Talbert, M.K., Miller, B.W., Morisette, J.T., 2017. Designing ecological climate change impact assessments to reflect key climatic drivers. Global Change Biology 23, 2537–2553. https://doi.org/10.1111/gcb.13653

Srikrishnan, V., Lafferty, D.C., Wong, T.E., Lamontagne, J.R., Quinn, J.D., Sharma, S., Molla, N.J., Herman, J.D., Sriver, R.L., Morris, J.F., Lee, B.S., 2022. Uncertainty Analysis in Multi-Sector Systems: Considerations for Risk Analysis, Projection, and Planning for Complex Systems. Earth's Future 10, e2021EF002644. https://doi.org/10.1029/2021EF002644

Subyani, A.M., 2019. Climate variability in space-time variogram models of annual rainfall in arid regions. Arab J Geosci 12, 650. https://doi.org/10.1007/s12517-019-4836-8

Thornton, P.E., Shrestha, R., Thornton, M., Kao, S.-C., Wei, Y., Wilson, B.E., 2021. Gridded daily weather data for North America with comprehensive uncertainty quantification. Sci Data 8, 190. https://doi.org/10.1038/s41597-021-00973-0

Thrasher, B., Wang, W., Michaelis, A., Melton, F., Lee, T., Nemani, R., 2022. NASA Global Daily Downscaled Projections, CMIP6. Sci Data 9, 262. https://doi.org/10.1038/s41597-022-01393-4

Ullrich, P.A., Xu, Z., Rhoades, A. m., Dettinger, M. d., Mount, J. f., Jones, A. d., Vahmani, P., 2018. California's Drought of the Future: A Midcentury Recreation of the Exceptional Conditions of 2012–2017. Earth's Future 6, 1568–1587. https://doi.org/10.1029/2018EF001007

Vano, J., Hammon, J., Gutmann, E., Wood, A., Mizukami, N., Clark, M., Pierce, D.W., Cayan, D., Wobus, C., Nowak, K., Arnold, J., 2020. Comparing Downscaled LOCA and BCSD CMIP5 Climate and Hydrology Projections: Release of Downscaled LOCA CMIP5 Hydrology. U.S. Bureau of Reclamation.

Walton, D.B., Hall, A., Berg, N., Schwartz, M., Sun, F., 2017. Incorporating Snow Albedo Feedback into Downscaled Temperature and Snow Cover Projections for California's Sierra Nevada. Journal of Climate 30, 1417–1438. https://doi.org/10.1175/JCLI-D-16-0168.1

Wayand, N.E., Hamlet, A.F., Hughes, M., Feld, S.I., Lundquist, J.D., 2013. Intercomparison of Meteorological Forcing Data from Empirical and Mesoscale Model Sources in the North Fork American River Basin in Northern Sierra Nevada, California. Journal of Hydrometeorology 14, 677–699. https://doi.org/10.1175/JHM-D-12-0102.1

Wood, A.W., Leung, L.R., Sridhar, V., Lettenmaier, D.P., 2004. Hydrologic Implications of Dynamical and Statistical Approaches to Downscaling Climate Model Outputs. Climatic Change 62, 189–216. https://doi.org/10.1023/B:CLIM.0000013685.99609.9e

Xue, Y., Janjic, Z., Dudhia, J., Vasic, R., De Sales, F., 2014. A review on regional dynamical downscaling in intraseasonal to seasonal simulation/prediction and major factors that affect downscaling ability. Atmospheric Research 147–148, 68–85. https://doi.org/10.1016/j.atmosres.2014.05.001